On the geometrical origin of the anisotropy in extrusion-based 3d printed structures

Romain Mesnil, Valentin Poussard, Karam Sab, Jean-François Caron

On the geometrical origin of the anisotropy in extrusion-based 3d printed structures

Romain Mesnil[a], Valentin Poussard[a], Karam Sab[b], Jean-François Caron[b]

[a] *École des Ponts ParisTech, Marne-La-Vallée, France*
[b] *Laboratoire Navier, UMR 8205, École des Ponts, IFSTTAR, CNRS, UPE, Marne-La-Vallée, France*

Abstract

Structures that are 3D printed by an extrusion process have periodic geometrical heterogeneity whose influence on the final stiffness properties is not extensively discussed in the existing literature. The objective of this article is to quantify the effect of local lace geometry on the anisotropy of extrusion-based 3d printed structures. A numerical homogenisation scheme is implemented to compute an equivalent homogeneous Kirchhoff-Love plate stiffness. The methodology is applied to the parametric study of an oblong lace resulting from *oriented-lace pressing*. The study reveals that the bending stiffness in the two principal directions may vary by an order of magnitude for common lace geometries, even in the assumption of a perfect bound between layers.

Numerical benchmarks against 3D Finite Element Analysis show that the proposed approach is accurate while significantly decreasing the number of degrees of freedom of the numerical model. Beyond understanding of geometrical defects on the overall stiffness of 3D printed structures, this approach can thus be applied for efficient structural analysis of 3D printed pieces with thousands of layers.

Keywords: Homogenisation, oriented lace pressing, 3D concrete printing, Shell theory

1. Introduction

1.1. Context

3D printed structures are fabricated by the successive deposition of material, in a layered manufacturing process. This deposition can be achieved with different techniques, including extrusion, or powder bed printing. In the construction industry, Pegna [1] proposed freeform construction through additive manufacturing as a new field of investigation. Extrusion is by far the most common process found nowadays in 3D concrete printing, in the followings of pioneering work by B. Khoshnevis's Contour Crafting [2] and by the University of Loughborough [3].

Figure 1: Concrete sample obtained by layer-wise extrusion. Geometrical heterogeneity (layering) is clearly visible, with $H = 6$mm, $B = 20$mm *(Photo: Leo Demont)*.

The layerwise nature of 3D printing naturally prompts the question of anisotropy of the resulting structures. This anisotropy has been experimentally measured on 3D printed samples, with a heavy focus on inter-layer strength in the concrete 3D-printing community [4]. The anisotropy may have two origins:

- Material anisotropy: the material properties are modified by the deposition process (stretching, phase change, etc.)
- Geometrical anisotropy: the geometry of the filaments induces a non-homogenous distribution of the material

A geometrical origin for anisotropy due to thickness variation has nonetheless been recently highlighted in 3D printed steel structures by Margerit *et al.* [5]. Structures obtained by an extrusion process with a circular nozzle, like some 3D printed concrete structures, exhibit more geometrical irregularities than those studied in [5]. This is illustrated in Figure 2, where the heterogeneity is not negligible compared to the wall thickness. Concrete printing by extrusion does not involve phase change, leaving cold joints as one of the main sources of material heterogeneity between layers. Poor interfaces behaviour, which might come from the microstructure of the interface itself has been studied in previous publications, like Nerella *et al.* [6]. However, proper mix formulation and inter-layer time can be adjusted to avoid weak interfaces, as suggested by Roussel [7]. Therefore, the geometrical origin of anisotropy in concrete or clay 3D printing cannot be disregarded as easily as in the conventional Fused Deposition Modelling process.

1.2. Previous work

1.2.1. Extrusion process for concrete printing

There is a continuum of strategies for extruding cementitious materials, which depend on the paste rheological properties, but it is possible to describe two asymptotical cases [8].

- *Extruded lace shaping* or *infinite brick extrusion* is a printing strategy in which a lace is extruded, and left undeformed after deposition. It relies on a high yield stress of the fresh mortar. This strategy is widespread and has been used on large-scale projects, for example by the team of TU Eindhoven [9].

- *Oriented Lace Pressing* relies on the deformation of the lace, which allows to control the layer height. This can be achieved with a mortar with low-yield stress and accelerator, as done by the company XTreeE [10], or with a mortar with high yield stress and a long printing time allowing structuration of the mix.

Both strategies have their own benefits depending on their context of application. For example, when printing overhangs, the *oriented lace pressing* strategy offers more possibility, beyond simple corbel [11].

1.2.2. Lace geometry

While *extruded-lace shaping* mainly relies on high yield stress to maintain the shape of the laces, *oriented-lace shaping* implies a deformation of laces. The lace geometry depends on kinematic parameters (extrusion and robotic speed, flow rate) and material parameter (yield stress, viscosity). Comminal *et al.* have simulated the deposition of viscous materials and proposed simplified lace cross-sections, including elliptical, cuboid and oblong shapes [12]. They later validated their model experimentally in [13]. Carneau et al. [14] have extended this study to yield stress fluids and experimentally measured that the oblong model is compatible with the mass conservation equation and measurements of the laces width and height. The typical lace geometry, which is studied in the followings of this article is shown in Figure 2.

Recently, those simple models for lace geometry have been proposed in [15], which proposed effective Young modulus depending on lace geometry and based on experimental measurements. This article proposes a more theoretical point of view, which complements this work.

1.2.3. Structural modelling for 3D printed-concrete

It should be noted that most 3D printed concrete structures are thin wall structures, with a wall thickness B in the centimeter range whereas other characteristic lengths (L_0, L_1) are in the metric range [16, 17]. It is therefore natural to rely on Kirchhoff-Love plate theory, which makes the assumption that the normal

Figure 2: A crushed sample of 3d printed concrete exhibiting the oblong lace geometry (contour highlighted by the authors)

of the mid-plane of the plate remains normal after transformation. Isotropic Kirchhoff-Love plate models have already been proposed to simulate the printing process of concrete structures and have shown good agreement with experimental data [18, 19]. The Kirchhoff-Love theory has the advantage to be simple to implement in Finite Element Modelling, but maybe more importantly, to provide engineers with intuitive generalised forces and moments instead of the local 3D strains and stresses.

Other recent work focus on mechanical modelling of 3D printed structures with voxelisation and 3D elements [20, 21]. While this approach is precise (when the voxel dimension is sufficiently small), it can be argued that it risks to scale poorly for models of components with several hundreds of layers compared to an equivalent Kirchhoff-Love plate model. This approach also makes it more difficult to identify the role of different geometrical or material parameters on the structural performance, since the notion of generalised force or moment is lacking in 3D modelling.

1.3. Homogenisation of periodic plates

It is well-known since the 1980's that a 3D plate which is periodic in its in-plane directions can be modelled as a 2D homogeneous Kirchhoff-Love plate if its thickness and the heterogeneity typical length are of the same order of magnitude, and if they are very small in comparison with the in-plane typical length of the plate.

The homogenisation problem can be summed up as follows: "Considering a given heterogeneous microstructure, how the overall properties of an equivalent homogeneous medium can be obtained?". One can find in [22], and the references cited in this monograph, the theoretical justifications of this homogenisation process and the methodology for the determination of the homogenised plate Kirchhoff-Love elastic stiffness tensors in terms of the 3D elastic properties of the unit-cell that generates the 3D periodic plate. To sum up the method, in the case of a periodic plate, it is based on the energy equivalence between the 3D medium and the plate model.

Figure 3 shows some examples of application of periodic homogenisation. in the scientific literature. The homogenisation can be applied to evaluate the stiffness properties of a structure, which is the focus of this article, but also to evaluate the load-bearing capacity of periodic structures, such as masonry structures. In a design context, periodic homogenisation is also applied to curved structures, which are not periodic *stricto sensu*, it offers however sufficient accuracy and considerably speeds up optimisation routines, as illustrated in [23, 24].

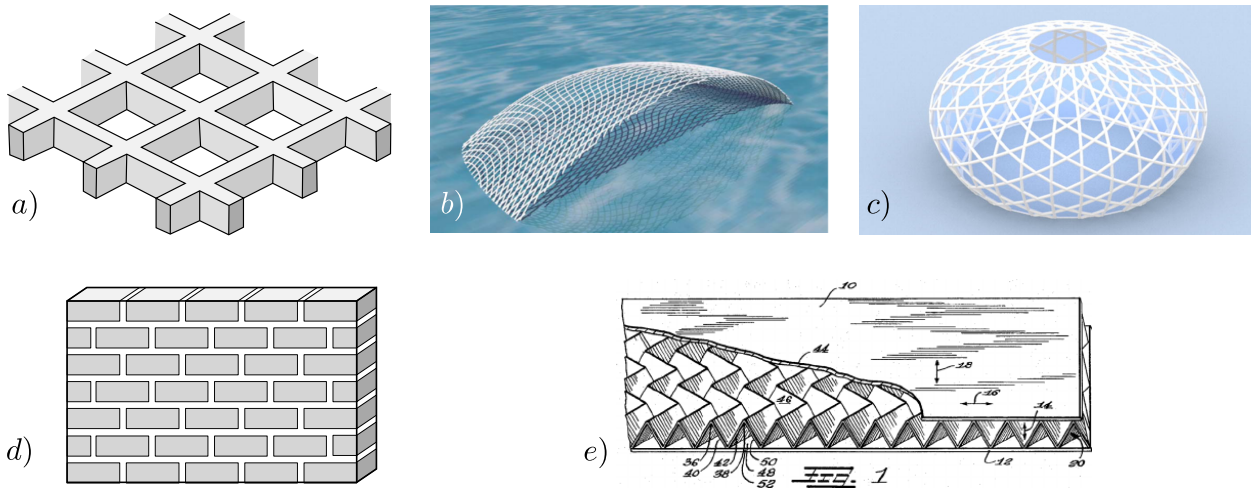

Figure 3: Examples of homogenised structures: a) beam lattice [25] , b) quadrangular gridshells [23], c) Kagome gridshells [24], d) masonry walls [26], e) sandwich panels [27].

1.4. Problem statement

The aim of this article is to use the homogenisation of periodic plates to estimate the anisotropy of 3D printed structures in the assumption of a perfectly homogeneous material. To do so, an equivalent homogeneous plate model is constructed: it allows the access to axial and bending stiffness and to easily interpret the influence of geometrical parameters on the behaviour of 3D printed structures. The result is a model allowing to interpret the contribution of the sole geometrical imperfection on the stiffness of 3D printed thin shell structures. Since the model considers a homogeneous material without softening defects, it constitutes therefore an upper bound on the stiffness that could be expected from a 3D printed sample. The homogenised model retains however practical relevance, both for the modelling of structures in the dry and fresh state.

The first section has introduced relevant literature and problem statement. The second section presents the research methodology with a summary of periodic plate homogenisation. The third section specifies the periodic domain studied and introduces the non-dimensional parameters describing the geometry of the laces. The fourth section sums up the results of numerical simulations and compares them to the analytical bounds previously found.

2. Methodology

2.1. Constitutive equations in Kirchhoff-Love plate theory

We consider a linear elastic plate with mid-plane $\mathcal{S}$. The plate fields are described using coordinates (x_1, x_2, x_3) and frame $(\mathbf{e_1}, \mathbf{e_2}, \mathbf{e_3})$, where $\mathbf{e_3}$ is orientated along the thickness direction which is normal to

the mid-plane. The displacement of the mid-plane is the 3-component vector $\boldsymbol{U}(x_1, x_2)$. The notations for the frames are shown in Figure 4.

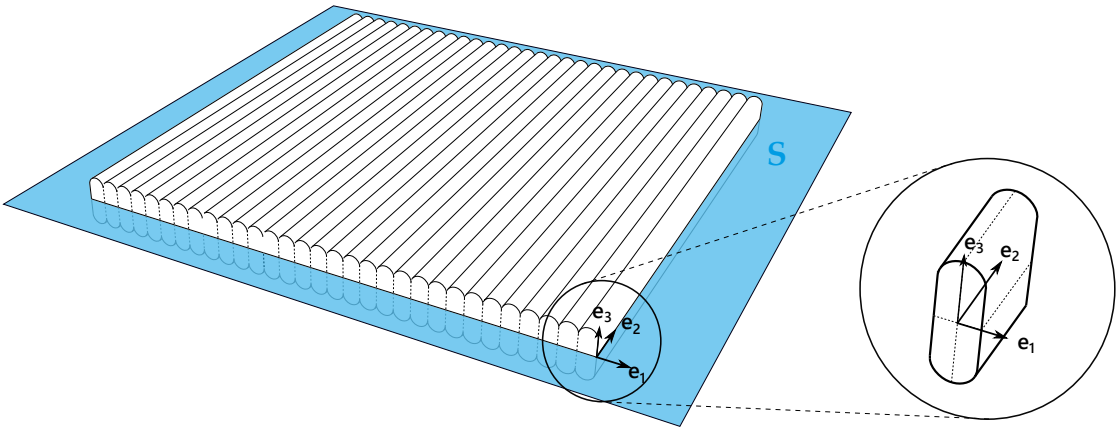

Figure 4: Depiction of a periodic plate and notations for frames in this article

The membrane forces $N_{\alpha\beta}(x_1, x_2)$[1] and bending moments $M_{\alpha\beta}(x_1, x_2)$ are the usual generalised stresses of plate theory. Their respective dual strain variables are the classical membrane strain $E_{\alpha\beta}(x_1, x_2)$ and curvature $\chi_{\alpha\beta}(x_1, x_2)$

$$\begin{cases} E_{\alpha\beta} = \dfrac{1}{2}\left(U_{\beta,\alpha} + U_{\alpha,\beta}\right) \\ \chi_{\alpha\beta} = -U_{3,\alpha\beta} \end{cases} \tag{1}$$

It will be shown that the considered periodic cell has two planes of symmetry, which means that there is no membrane-bending coupling [22]. Considering the $(\mathbf{e_2}, \mathbf{e_3})$ or $(\mathbf{e_3}, \mathbf{e_1})$ plane symmetry and the invariance property of strain energy, we have :

$$A_{1112} = A_{2212} = D_{1112} = D_{2212} = 0 \tag{2}$$

The simplified constitutive equations in Kirchhoff-Love orthotropic plate theory are recalled in equation (3) and (4). There are in general 12 parameters of a orthotropic elastic Kirchhoff-Love plate, due to the symmetry of the stiffness matrix. For a uniform material distribution, this number of parameters is reduced

[1] Greek letters indicate that the subscript index can take either the value 1 or 2.

to 5 (E_1,E_2,ν_{12}, G_{12}, and thickness).

$$\begin{pmatrix} N_{11} \\ N_{22} \\ N_{12} \end{pmatrix} = \begin{pmatrix} A_{1111} & A_{1122} & 0 \\ A_{1122} & A_{2222} & 0 \\ 0 & 0 & 2A_{1212} \end{pmatrix} \cdot \begin{pmatrix} E_{11} \\ E_{22} \\ E_{12} \end{pmatrix} \tag{3}$$

$$\begin{pmatrix} M_{11} \\ M_{22} \\ M_{12} \end{pmatrix} = \begin{pmatrix} D_{1111} & D_{1122} & 0 \\ D_{1122} & D_{2222} & 0 \\ 0 & 0 & 2D_{1212} \end{pmatrix} \cdot \begin{pmatrix} \chi_{11} \\ \chi_{22} \\ \chi_{12} \end{pmatrix} \tag{4}$$

Equations (3) and (4) can be written in matrix form as $\mathbf{N} = \mathbf{AE}$ and $\mathbf{M} = \mathbf{D}\boldsymbol{\chi}$. The plate strain energy (surface) density is given by equation (5). It is strictly positive unless $\boldsymbol{N}$ and $\boldsymbol{M}$ are both null.

$$W = \frac{1}{2}\boldsymbol{E}^T.\boldsymbol{A}.\boldsymbol{E} + \frac{1}{2}\boldsymbol{\chi}^T\boldsymbol{D}.\boldsymbol{\chi} \tag{5}$$

2.2. Summary of the homogenisation procedure

Periodic homogenisation is applied to micro-structures with invariance by translation. In Figure 4, the micro-structure is periodic along $\mathbf{e_1}$ and $\mathbf{e_2}$. The smallest periodic sub-cell is written Y. It assumed that all characteristic lengths of Y are small compared to the dimensions of the plate, i.e. when the number of cells is large. The objective of homogenisation is to create a consistent equivalent plate model, in the sense that strain energy of the plate model converges towards the one of the micro-structure when the number of cells increases.

It will be shown that the considered periodic cell Y, whose geometry is shown in Figure 4, of dimensions l_1,l_2,l_3 has two planes of symmetry with an isotropic material. In this case, it is possible to reduce the problem to a portion of cell Y_0 delimited by the two planes of symmetry. The periodic cell and boundary conditions for Love-Kirchhoff plates are presented in [22] and recalled in Figure 5. Note that notations for cell dimensions of Figure 5 are identical to [22], usual notations found in the literature on 3D printing [12, 28] are $l_1 = B$, $l_2 = L$ and $l_3 = H$.

Generalised forces in the cell are defined by equation (6). In the followings, the notation $\langle\ .\ \rangle$ denotes an average. We introduce S_{Y_0}, the surface area of the middle surface of the cell. With the notations of Figure

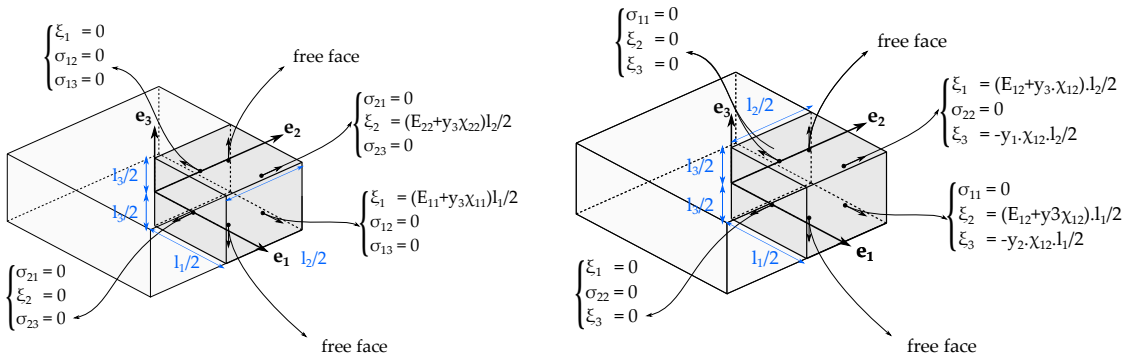

(a) symmetric loads

(b) Skew symmetric loads.

Figure 5: Boundary conditions applied to a periodic cell with two planes of symmetry.

5, $S_{Y_0} = \frac{l_1 l_2}{4}$.

$$\begin{cases} N_{\alpha\beta} = \langle \sigma_{\alpha\beta} \rangle = \dfrac{1}{S_{Y_0}} \displaystyle\int_{Y_0} \sigma_{\alpha\beta} \mathrm{d}V \\ M_{\alpha\beta} = \langle x_3 \sigma_{\alpha\beta} \rangle = \dfrac{1}{S_{Y_0}} \displaystyle\int_{Y_0} \sigma_{\alpha\beta} x_3 dV \end{cases} \tag{6}$$

General displacements can be defined in a similar manner:

$$\begin{cases} E_{\alpha\beta} = & \dfrac{1}{B} \langle \varepsilon_{\alpha\beta} \rangle \\ \chi_{\alpha\beta} = & \dfrac{12}{B^3} \langle x_3 \varepsilon_{\alpha\beta} \rangle \end{cases} \tag{7}$$

The homogenisation procedure requires the solution of elasticity problem (8) solved for the appropriate boundary conditions represented in Figure 5.

$$\begin{cases} \mathbf{div}\boldsymbol{\sigma} = \mathbf{0} \\ \boldsymbol{\sigma} = \boldsymbol{C}\left(\boldsymbol{x_1}, \boldsymbol{x_2}, \boldsymbol{x_3}\right) : \boldsymbol{\varepsilon} \\ \boldsymbol{\varepsilon} = \boldsymbol{\nabla_s} \boldsymbol{\xi} \\ \text{boundary conditions from Figure 5} \end{cases} \tag{8}$$

The solution of an elasticity problem allows to compute generalised forces associated to generalised displacements. Computing the average of the stress fields through the stiffness of the plate (along $\mathbf{e_3}$) should be enough to determine the equivalent stiffness matrix, however this is not trivial in Finite Element Software. Therefore, we use the elastic strain energy W of the elasticity problem and identify it to the strain energy W_{hom} associated with the macroscopic field $W = W_{hom}$.

2.3. Numerical homogenisation

The Finite Element Software Abaqus is used to solve the static problems over the sub-cell Y_0. For each problem, total strain energy is computed and divided by the middle surface of the sub-cell, $HL/2$, in order to obtain plate strain energy W_{hom}. Application of the Hill-Mandel principle yields equality between the microscopic energy computed by the finite element analysis and the macroscopic energy. It will be shown in the next section that we have to determine at most eight coefficient, since energy depends linearly on the coefficients of the stiffness matrices $\mathbf{A}, \mathbf{B}, \mathbf{D}$: eight well-chosen problems are thus enough to construct the homogenised stiffness matrix.

The periodic subcell is modelled as a parallelepiped. For the sake of applying proper boundary conditions, the Finite Element Model uses two materials, shown in Figure 6. The constitutive material of the cell, shown in light blue in the image, has a Young Modulus $E = 1$ MPa. The second material, shown in a darker blue in the image is used to represent voids and has a Young modulus $E = 10^{-6}$MPa. With such a small value, its influence on total strain energy is negligible. This is indeed verified in the section discussing the results.

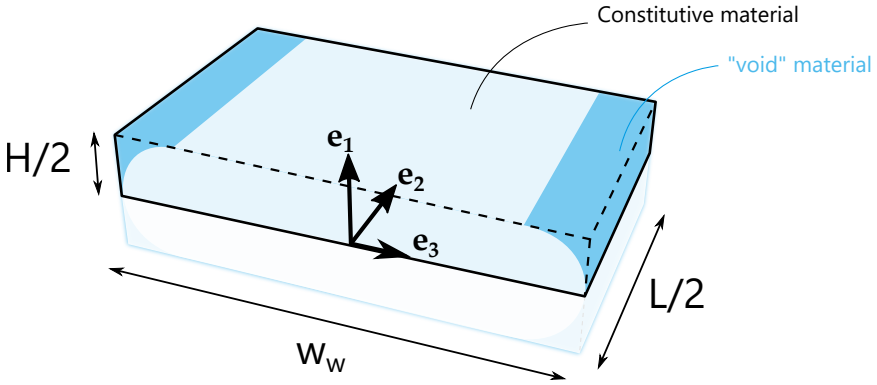

Figure 6: The unit cell Y_0, as modelled in Abaqus with constitutive material in light blue and *void material* in darker. The mirror image of the Y_0 cell is represented in transparency.

2.4. Load cases

This section introduces now the eight load cases used to determine the A_{ijkl} and the D_{ijkl} coefficients. The boundary conditions associated to the macroscopic fields $E_{\alpha\beta}$ and $\chi_{\alpha\beta}$ applied to the periodic cell are shown in Figure 5. No internal forces are applied. The total elastic strain energy W_{tot} is computed numerically over the sub-cell geometry Y_0 for each loading case. To get surface strain energy defined in equation (5), we divide its value by $S_{Y_0} = HL/4$, the area of the middle surface of subcell Y_0.

$$W_{hom} = \frac{4W_{tot}}{HL} \tag{9}$$

	E_{11}	E_{22}	E_{12}	χ_{11}	χ_{22}	χ_{12}	W_{hom}
Problem 1	1	0	0	0	0	0	$\frac{1}{2}A_{1111}$
Problem 2	0	1	0	0	0	0	$\frac{1}{2}A_{2222}$
Problem 3	0	0	1	0	0	0	$2A_{1212}$
Problem 4	1	1	0	0	0	0	$\frac{1}{2}\left(A_{1111}+A_{2222}+A_{1122}\right)$
Problem 5	0	0	0	1	0	0	$\frac{1}{2}D_{1111}$
Problem 6	0	0	0	0	1	0	$\frac{1}{2}D_{2222}$
Problem 7	0	0	0	0	0	1	$2D_{1212}$
Problem 8	0	0	0	1	1	0	$\frac{1}{2}\left(D_{1111}+D_{2222}+D_{1122}\right)$

Table 1: Strain energy associated to each subproblem solved with the finite element method and its relation to macroscopic stiffness coefficients.

Table 1 sums up the different elasticity problems solved with the finite element method (i.e. which boundary conditions are applied), and the relation between strain energy of the cell and macroscopic stiffness coefficients obtained by application of equation (5).

2.5. Polynomial fitting

The finite element method allows to solve the homogenisation problems for specific lace geometries. Rather than solving the homogenisation problem for any possible lace geometry, a structural engineer might be more inclined to use a pseudo-analytical formula in order to define the equivalent plate model. We propose thus a simple and realistic parametrisation of lace shapes allowing to perform polynomial fitting of numerical results.

The overall methodology for constructing a plate model has been presented. The next section introduces the relevant parameters describing a simplified geometrical model of laces.

3. Problem description: oriented lace pressing

3.1. Periodic homogenisation procedure

Figure 7 displays a cross-section of a 3D printed wall using the oblong lace geometry. It has been experimentally demonstrated that this shape is close to the actual lace shape resulting from *Oriented Lace Pressing* [12, 14, 15], and it has the benefit to be described with few geometrical parameters. The geometry is invariant along $\mathbf{e_2}$, and the cell highlighted in the blue rectangle in the image is periodic along $\mathbf{e_1}$.

The periodic cell Y is depicted more precisely in Figure 8. It is an oblong shape, with a rectangular cross-section of width w_b and height H connected to two elliptical caps, each of width $w_c/2$, extruded along $\mathbf{e_2}$. The wall width w_w is simply defined as $w_w = w_b + w_c$. The independent shape parameters describing

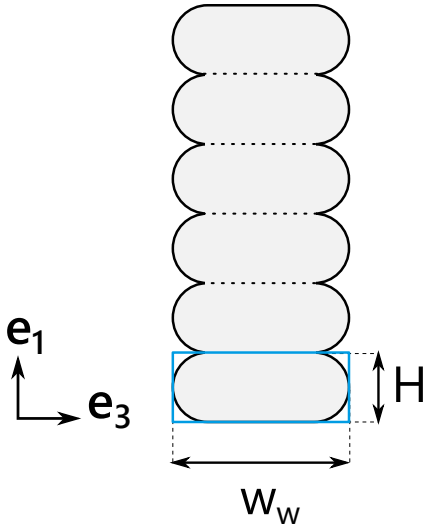

Figure 7: Cross-section of a 3D-printed wall and identification of a cell that is periodic in $\mathbf{e_2}$ and invariant along $\mathbf{e_1}$.

the cell are thus its height H, and the bond width and the wall width of the section w_w. The material parameters are the Young modulus E and Poisson's ratio ν.

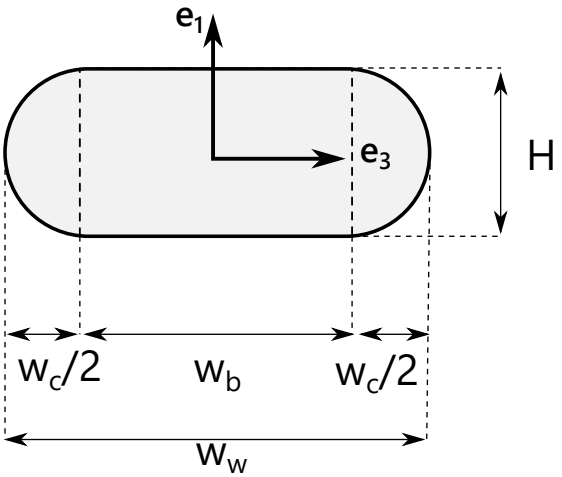

Figure 8: Geometry of the unit periodic cell

3.2. Non-dimensional analysis: parameters

In the followings, non-dimensional parameters are used to describe the cell geometry and the stiffness: $H^* = H/w_w$ is the cell aspect ratio, $w^* = w_b/w_w$ is the normalised bond width, whereas $L^* = L/H$ is the length ratio. However, since the cell is invariant along $\mathbf{e_2}$ and since L can be arbitrarily chosen, all non-dimensional numbers are independent of L^*. Intuitively, the stiffness is governed by the normalised bond width: for $w^* = 1$, the plate is a uniform plate, whereas for $w^* = 0$, the lace would be independent.

The bond width was observed to be a key factor in the axial stiffness in experiments by Fang *et al.* [15]. In order to keep the study as simple as possible, the simplest geometrical model for the lace, used for example by Comminal *et al.* [12], is chosen. Namely the parametric study is restricted to the case $H = w_c$, where the caps are circular. With the non-dimensional parameters, this equality reads as $H^* = 1 - w^*$.

The constitutive material is here modelled as linear, elastic and isotropic, and can thus be described with Young Modulus E and ν. Note that $\mathbf{A}$ and $\mathbf{D}$ are obviously proportional to the Young modulus, because for each auxiliary problem, only two numbers are expressed in Newtons. Therefore, there is no need to vary the Young modulus in the numerical study and there are only two independent non-dimensional input parameters describing each auxiliary problem: ν and w^*.

Table 2 shows the different values for w^* and ν considered in the numerical study.

Name	Symbol	Values
Poisson's ratio	ν	$[0.15, 0.2, 0.25, 0.3]$
Normalised bond width	w^*	$[0.05, 0.25, 0.5, 0.75, 0.95]$
Aspect ratio	H^*	$1 - w^*$

Table 2: Non-dimensional parameters for the study

The values of w^* were chosen to evenly map the possible range of parameters. The corresponding shapes are shown in Figure 9. The practical values for w^* might vary with the chosen material and process, a more detailed view on concrete printing is proposed in the discussion.

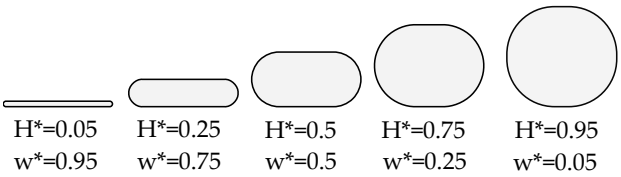

Figure 9: Lace shapes considered in the parametric study

The geometry of the lace converges to the one of uniform plate when $w^* \longrightarrow 1$. Indeed, it can be seen that the volume of material $\mathcal{V} = \pi H^2 L + w_b H L$ converges towards the volume of the bounding box $\mathcal{V}_{box} = w_w H L$.

$$\frac{\mathcal{V}}{\mathcal{V}_{box}} = \frac{\pi H}{w_w} + \frac{w_b}{w_w} = \pi \left(1 - w^*\right) + w^*$$

Therefore, the heterogeneity of the microstructure is a decreasing function of w^*, and the homogenised model is expected to converge towards the isotropic plate properties when limit w^* tends to unity.

3.3. Non-dimensional analysis: results

The components of the non-dimensional stiffness matrix $\mathbf{A}^*$ and $\mathbf{D}^*$ are constructed from the stiffness of a uniform plate of thickness B, for which there are analytical expression. A non-dimensional number equal to 1 means that the term of the stiffness matrix is equal to the one of a uniform plate of thickness B. Note again that $\mathbf{A}$ and $\mathbf{D}$ are obviously proportional to the Young modulus, and that all coefficients of $\mathbf{A}^*$ and $\mathbf{D}^*$ should be inferior to 1, the uniform plate of thickness B being stiffer than the structures studied here. Other scaling could be used, for example by comparing with the stiffness of a plate of width w_b, which constitutes a lower bound to the stiffness of the actual structure.

$$\begin{cases} A^*_{1111} = \dfrac{A_{1111}\left(1-\nu^2\right)}{EB} \\ A^*_{2222} = \dfrac{A_{2222}\left(1-\nu^2\right)}{EB} \\ A^*_{1122} = \dfrac{A_{1122}\left(1-\nu^2\right)}{\nu EB} \\ A^*_{1212} = \dfrac{2A_{1212}\left(1+\nu\right)}{EB} \\ D^*_{1111} = \dfrac{12D_{1111}\left(1-\nu^2\right)}{EB^3} \\ D^*_{2222} = \dfrac{12D_{2222}\left(1-\nu^2\right)}{EB^3} \\ D^*_{1122} = \dfrac{12D_{1122}\left(1-\nu^2\right)}{\nu EB^3} \\ D^*_{1212} = \dfrac{24D_{1212}\left(1+\nu\right)}{EB^3} \end{cases} \tag{10}$$

3.4. Analytical relations between coefficients of the stiffness matrix

The problems defined in Table 1 do not have an obvious analytical solution, and numerical study remains necessary to evaluate the stiffness A_{ijij} and D_{ijij}. However, it is possible to construct an exact analytical solution that will highlight coupling between the different terms of the stiffness matrix.

To do so, we consider stress fields in the form of equation (11), which are statically compatible. Indeed, they are at equilibrium ($\mathrm{div}\sigma = \mathbf{0}$) and continuity of $\sigma \cdot \mathbf{n}$.

$$\forall\,(\alpha,\beta) \in \mathbb{R}^2,\ \sigma = \begin{pmatrix} 0 & 0 & 0 \\ 0 & \alpha+\beta x_2 & 0 \\ 0 & 0 & 0 \end{pmatrix} \tag{11}$$

The associated membrane force are given by equation (12), the quantity S, which is the cross-sectional area

of the lace is introduced.

$$\begin{pmatrix} N_{11} \\ N_{22} \\ N_{12} \end{pmatrix} = \begin{pmatrix} \frac{1}{H}\int_{\mathcal{Y}} \sigma_{11} dV \\ \frac{1}{H}\int_{\mathcal{Y}} \sigma_{22} dV \\ \frac{1}{H}\int_{\mathcal{Y}} \sigma_{12} dV \end{pmatrix} = \begin{pmatrix} 0 \\ \alpha S/H \\ 0 \end{pmatrix} \tag{12}$$

and the associated bending moment is given by equation (13). The notation I stands for the second moment of inertia I_1 of the cell geometry in the $(\mathbf{e_1}, \mathbf{e_3})$ plane. The analytical value of I and its derivation are detailed in the appendix.

$$\begin{pmatrix} M_{11} \\ M_{22} \\ M_{12} \end{pmatrix} = \begin{pmatrix} \frac{1}{H}\int_{\mathcal{Y}} \sigma_{11} x_3 dV \\ \frac{1}{H}\int_{\mathcal{Y}} \sigma_{22} x_3 dV \\ \frac{1}{H}\int_{\mathcal{Y}} \sigma_{12} x_3 dV \end{pmatrix} = \begin{pmatrix} 0 \\ \beta \frac{I}{H} \\ 0 \end{pmatrix} \tag{13}$$

The strain field compatible with σ are given by equation (14).

$$\varepsilon = \begin{pmatrix} \frac{-\nu\sigma_{22}}{E} & 0 & 0 \\ 0 & \frac{\sigma_{22}}{E} & 0 \\ 0 & 0 & \frac{-\nu}{E}\sigma_{22} \end{pmatrix} \tag{14}$$

Application of equation (7) allows to construct macroscopic displacements and curvature $\mathbf{E}$ and χ.

$$\begin{pmatrix} E_{11} \\ E_{22} \\ E_{12} \\ \chi_{11} \\ \chi_{22} \\ \chi_{12} \end{pmatrix} = \frac{1}{E} \begin{pmatrix} -\alpha\nu \\ \alpha \\ 0 \\ -\beta\nu \\ \beta \\ 0 \end{pmatrix} \tag{15}$$

The strain field ε is kinematically admissible, since it satisfies following relation:

$$\varepsilon = \begin{pmatrix} E_{11} + \chi_{11} x_3 & 0 & 0 \\ 0 & E_{22} + \chi_{22} x_3 & 0 \\ 0 & 0 & 0 \end{pmatrix} + \nabla_s \begin{pmatrix} 0 \\ 0 \\ -\frac{\nu\alpha}{E} - -\frac{\nu\beta x_3}{2E} \end{pmatrix} \tag{16}$$

The fields σ, ε are respectively statically and kinematically admissible and they are compatible (related by the constitutive equations of an isotropic material). Therefore, $\mathbf{N}, \mathbf{M}$ are statically compatible, the macroscopic strains $\mathbf{E}, \chi$ are compatible with the stress and are also kinematically admissible. We have thus the solution of a problem of elasticity. Application of (3) and (4) yields relation between the terms of the

stiffness matrix.

$$\begin{pmatrix} 0 \\ N_{22} \\ 0 \end{pmatrix} = \begin{pmatrix} A_{1111} & A_{1122} & 0 \\ A_{1122} & A_{2222} & 0 \\ 0 & 0 & A_{1212} \end{pmatrix} \begin{pmatrix} -\nu E_{22} \\ E_{22} \\ 0 \end{pmatrix} \tag{17}$$

$$\begin{pmatrix} 0 \\ M_{22} \\ 0 \end{pmatrix} = \begin{pmatrix} D_{1111} & D_{1122} & 0 \\ D_{1122} & D_{2222} & 0 \\ 0 & 0 & D_{1212} \end{pmatrix} \begin{pmatrix} -\nu \chi_{22} \\ \chi_{22} \\ 0 \end{pmatrix} \tag{18}$$

Equations (17) and (18) are true for any value of E_{22} and χ_{22}. The solution of the linear system yields following equation:

$$\begin{cases} A_{1122} = & \nu A_{1111} \\ A_{2222} = & \nu^2 A_{1111} + \dfrac{ES}{H} \\ D_{1122} = & \nu D_{1111} \\ D_{2222} = & \nu^2 D_{1111} + \dfrac{EI}{H} \end{cases} \tag{19}$$

This equality can be written in terms of non-dimensional numbers.

$$\begin{cases} {A_{1111}}^* = & {A_{1122}}^* \\ {A_{2222}}^* = & \nu^2 {A_{1111}}^* + \dfrac{\left(1-\nu^2\right) S}{HB} \\ {D_{1111}}^* = & {A_{1122}}^* \\ {D_{2222}}^* = & \nu^2 {D_{1111}}^* + \dfrac{12I\left(1-\nu^2\right)}{HB^3} \end{cases} \tag{20}$$

These equations are exact relations between the coefficient of the stiffness matrix. Therefore, one is required to compute only four values (instead of eight in the general case) to get the whole stiffness matrix coefficients $A_{1111}, A_{12112}, D_{1111}, D_{1212}$.

4. Numerical results

The previous section highlights exact relations between the coefficients of the stiffness matrix, which decrease the number of numerical problems to solve down to four for each set of values of (H^*, ν). No assumption has been made on the exact geometry of the lace, besides central symmetry. This section presents the numerical results obtained with finite element analysis and to propose simple polynomial regressions that can readily be used.

4.1. Convergence of numerical model and analytical relations

Convergence studies on the mesh density have been conducted to guarantee the accuracy of the results of the Finite Element Analysis. The analytical results proposed in the previous section have been verified by solving the auxiliary problems for A_{2222}, A_{1122}, D_{2222}, D_{1122}, and by computing their expected values from equation (20). The agreement between numerical and analytical results is perfect (error inferior machine precision).It was also ensured that the equality are verified for $\nu = 0$, which proves that the "void" material chosen in the Finite Element simulation is indeed negligible.

As shown in 3.2, the limit case $w^* \longrightarrow 1$ corresponds to a uniform shell of thickness B, it is thus clear that all non-dimensional values ${A_{ijij}}^*$ and ${D_{ijij}}^*$ should converge to unity. This trend can also be observed on our numerical results. Therefore, we have enforced the fitting polynomials to take the value 1 for $w^* = 1$.

4.2. Numerical results on membrane stiffness

4.2.1. ${A_{1111}}^*$

The numerical results for ${A_{1111}}^*$ are shown in Table B.5, in the appendix. It appears that Poisson's ratio has very little influence on the values of this non-dimensional ratio. This observation is confirmed by the linear regression in w^* and ν, where the dependency in ν is obviously negligible compared to the one in H^*. We propose therefore the following linear fitting:

$$ {A_{1111}}^* \left(H^*, \nu\right) \simeq 0.19 + 0.81 w^* \tag{21} $$

The fitting is accurate, with $R^2 = 0.9998$ and a maximal error of 0.6% on the numerical results. Figure 10 shows the numerical values of ${A_{1111}}^*$ and the proposed linear fitting.

4.2.2. A_{2222}

The combination of equations (21) and (19) yields the approximation of ${A_{2222}}^*$ written in equation (22). Here, a term in $\nu^2 w^*$ appears from the analytical relation between A_{1111} and A_{2222}. The value of A_{2222} is therefore influenced by Poisson's ratio, but this influence remains limited.

$$ {A_{2222}}^* \left(H^*, \nu\right) \simeq 0.79 - 0.60\nu^2 + \left(0.21 + 0.60\nu^2\right) w^* \tag{22} $$

Figure 11 displays the ratio between A_{2222} and A_{1111}, together with its approximation constructed from equations (21) and (22). For $w^* = 0.5$, this ratio is close to 1.5, which means that axial stiffness in the

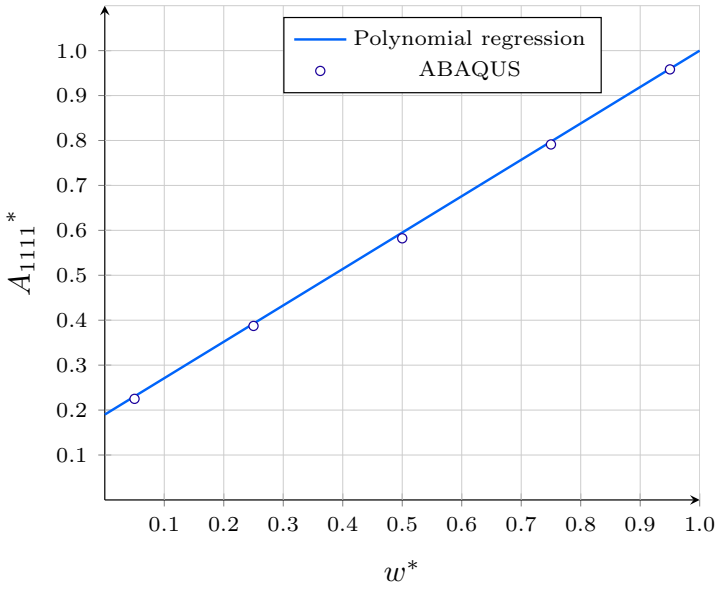

Figure 10: Numerical values for A_{1111} for $\nu = 0.3$ and the proposed linear regression.

longitudinal direction is 50% higher than in the transverse direction. This difference is significant, although no material heterogeneity is assumed.

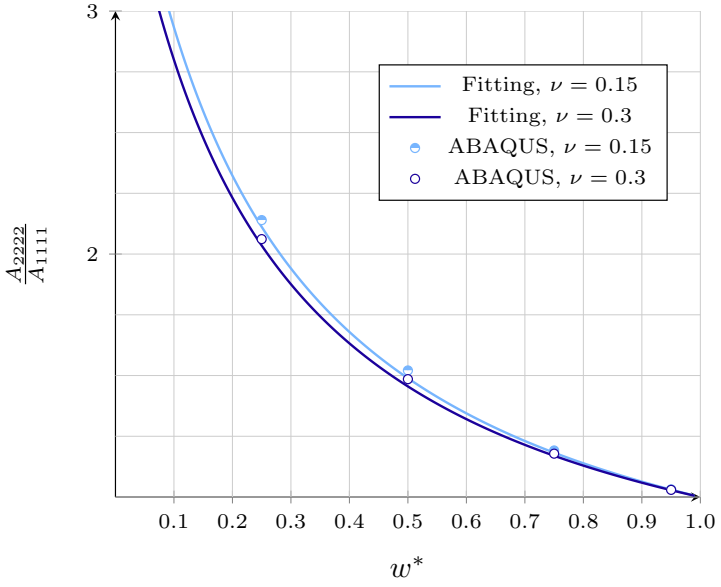

Figure 11: Ratio $\frac{A_{2222}}{A_{1111}}$ and regression from equation (22).

4.2.3. ${A_{1212}}^*$

The results on A_{1212} are similar to A_{1111} and are shown in Table B.6 in the appendix. Figure 12 shows the numerical results for $\nu = 0.3$ together with the proposed linear regression. The influence of Poisson's

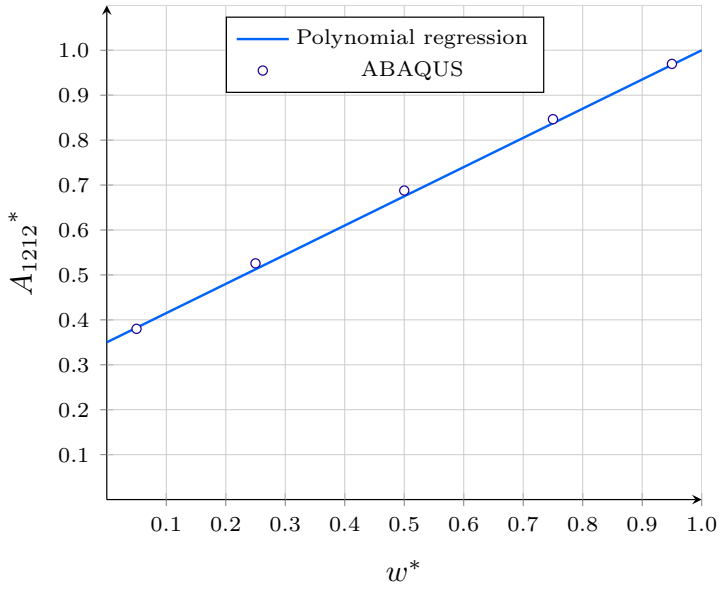

Figure 12: Numerical results for A_{1212} for $\nu = 0.3$ and linear regression in H^*.

ratio on ${A_{1212}}^*$ is negligible and a linear regression is proposed in equation (23).

$$ {A_{1212}}^* (H^*, \nu) \simeq 0.35 + 0.65 w^* \tag{23} $$

4.3. Numerical results on bending stiffness

4.3.1. ${D_{1111}}^*$

Figure 13 shows the numerical values for ${D_{1111}}^*$ for $\nu = 0.3$ together with various polynomial approximations. The observed trend is different from the one of membrane stiffness: ${D_{1111}}^*$ converges indeed to 0 as H^* converges to 1, which is in accordance with the intuition. Here, both quadratic and cubic regressions are proposed. The quadratic regression (dark blue curve) is accurate enough for a wide range of values of w^* but can yield negative values for w^* close to 0, which is not realistic. Constraining positive values for the quadratic regression is possible (light blue curve), but is not accurate for intermediate values of w^*.

Therefore, a cubic regression in H^* is proposed in equation (24). It is positive for $w^* > 0.04$, which falls

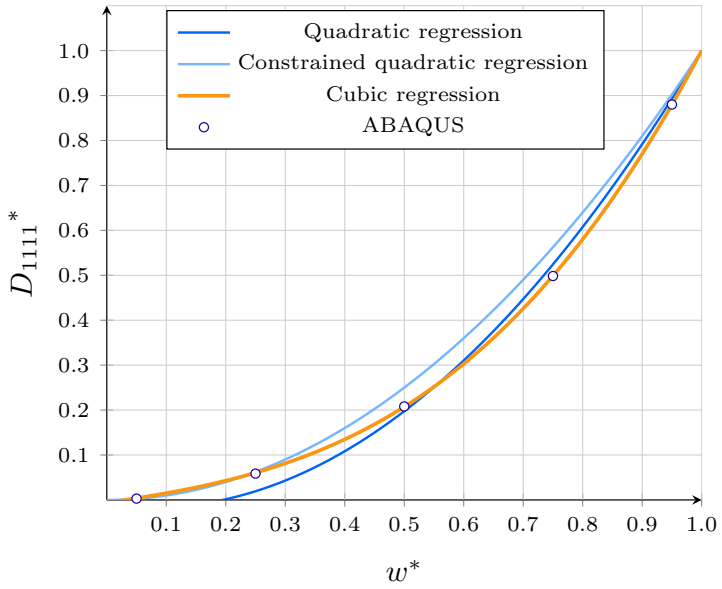

Figure 13: Numerical values for ${D_{1111}}^*$ for $\nu = 0.3$ and the proposed polynomial regressions.

well within the practical range of structures resulting from oriented lace pressing.

$$ {D_{1111}}^* \simeq -0.006 + 0.192w + 0.124w^2 + 0.69w^3 \tag{24} $$

4.3.2. ${D_{2222}}^*$

${D_{2222}}^*$ depends linearly on ${D_{1111}}^*$ and $\frac{12I}{HB^3}$. The analytical value of $\frac{12I}{HB^3}$ is given in the appendix: it turns out to be a cubic polynomial in H^*, so that a cubic regression for ${D_{2222}}^*$ can be constructed.

$$ {D_{2222}}^* \simeq \left(0.094 - 0.675\nu^2\right) + \left(1.718 + 3.851\nu^2\right) w^* - \left(1.362 + 3.811\nu^2\right) {w^*}^2 + \left(0.55 + 0.635\nu^2\right) {w^*}^3 \tag{25} $$

The ratio between ${D_{2222}}^*$ and ${D_{1111}}^*$ is displayed in Figure 14. The ratio is significant for a wide range of values of w^*. For example, for $w^* = 0.5$, this ratio is superior to 3. The ratio tends towards infinity when w^* goes to 0. The regression proposed with the cubic polynomial accurately predicts the relative longitudinal and transverse bending stiffness. In practice, the anisotropy of 3D printed structures can thus be significant, even under the assumption of uniform material. Although the geometrical origin of anisotropy in 3d printed structures is often overlooked, this simple comparison shows that the shape of the extruded lace may have an influence on the stiffness properties at the structural scale.

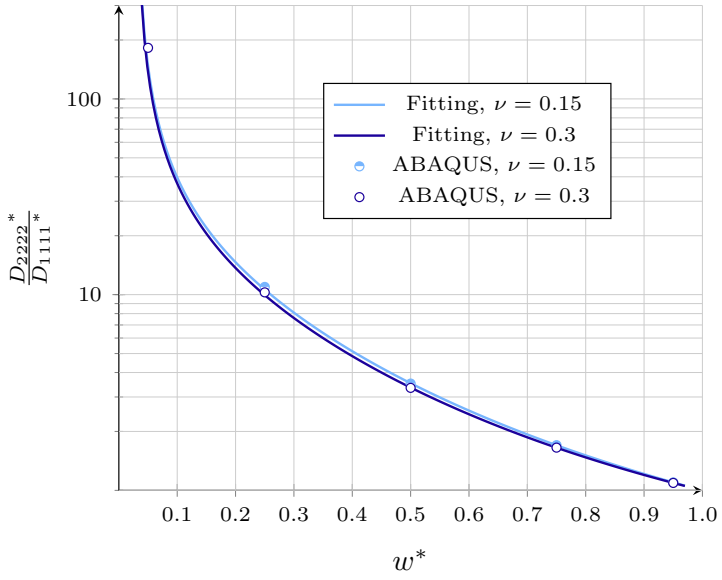

Figure 14: Ratio $\frac{D_{2222}}{D_{1111}}$ and regression.

4.3.3. ${D_{1212}}^*$

The results for ${D_{1212}}^*$ have similar trend to D_{1111}. They have very little sensibility to Poisson's ratio. The quadratic regression follows:

$$ {D_{1212}}^* \simeq 0.307 - 0.306w^* + 0.999{w^*}^2 \tag{26} $$

A cubic regression can also be proposed (${D_{1212}}^* \simeq 0.294 - 0.135w + 0.591w^2 + 0.25w^3$), but it doesn't fundamentally improves the results. Figure 15 shows numerical result for $\nu = 0.3$ together with the quadratic and cubic regressions. Both regressions are very close, which indicates that there is no over-fitting of the numerical data.

4.4. Synthesis of numerical results

This section has introduced the results of the parametric study with finite element analysis. The numerical results show that the dimensionless numbers have little sensitivity to Poisson's ratio ν, and polynomial fitting have been proposed. Linear regression is sufficient to accurately estimate axial stiffness, while quadratic or even cubic polynomials are required for bending stiffness. The proposed linear regressions for

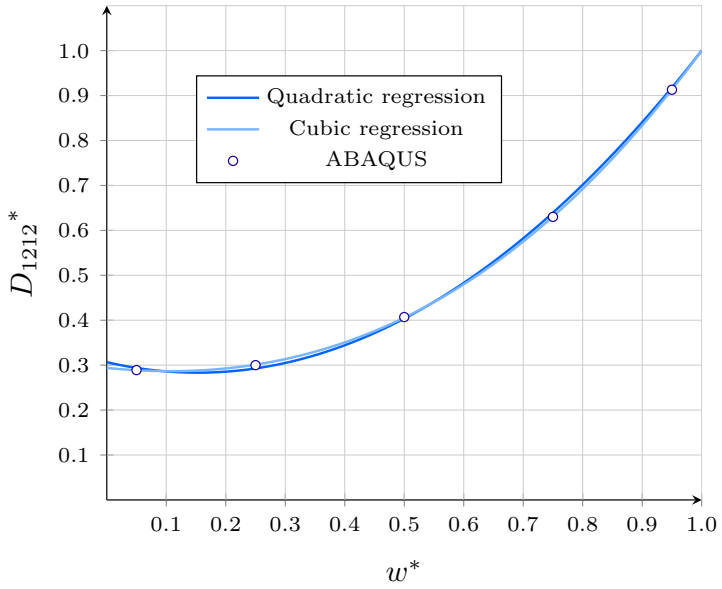

Figure 15: Numerical values for $D_{1212}{}^*$ for $\nu = 0.3$ and the proposed polynomial regressions.

membrane stiffness are recalled in equation (27).

$$\mathbf{A}^* = \begin{pmatrix} 0.19 + 0.81w^* & 0.19 + 0.81w^* & 0 \\ 0.19 + 0.81w^* & 0.79 - 0.6\nu^2 + \left(0.21 + 0.6\nu^2\right) w^* & 0 \\ 0 & 0 & 0.35 + 0.65w^* \end{pmatrix} \tag{27}$$

The polynomial regression for bending stiffness are recalled in equation (28).

$$\mathbf{D}^* = \begin{pmatrix} \text{eq.(24)} & \text{eq.(24)} & 0 \\ \text{eq.(24)} & \text{eq.(25)} & 0 \\ 0 & 0 & \text{eq.(26)} \end{pmatrix} \tag{28}$$

The polynomial regression of the coefficients of the stiffness matrix are different, which means that the homogenised stiffness cannot be described with an equivalent Young's Modulus or thickness, as sometimes seen in the literature.

5. Comparative study

The previous section has presented the numerical results and introduced polynomial regression for the stiffness matrices **A** and **D**. The aim of this section is to discuss the application of the homogenisation

method to the structural analysis of 3d printed components by extrusion. First a comparative study between a 3D brick model and an equivalent orthotropic shell computed with the method proposed in this article is presented. In order to illustrate the accuracy of the homogenisation, we apply this technique to a practical example: a cylinder similar to the one described in [29]. We perform finite-element analysis both for a 3D finite element and a homogenised plate finite element found with our regression formula.

5.1. Geometry and material properties

The cylinder has a diameter of 35cm, a height of 45cm, $H = 6$mm and $B = 12$mm. The Young's modulus is $E = 100$ kPa, similar to geopolymer used in [29] after one hour and Poisson's ratio is $\nu = 0.2$ and density is 2.5.

5.2. Load cases

Two load cases are considered:

- Load case 1: Self-weight
- Load case 2: Self-weight for a tilted cylinder with an angle of 5°

The first case has a practical interest, since it can model the printing process of the cylinder. Similar case studies have been performed, without considering geometrical heterogeneity in [30]. It is however obvious that most of the strain energy is due to the axial deformation of the cylinder, so that this load-case provides information mainly on the quality of approximation of A_{1111}.

The second load-case might be relevant for the 3d printing of cantilevers, but more importantly, it involves all the terms of the stiffness matrix.

5.3. Models

This study compares two models:

- A 3D model with C3D8R elements.
- A plate model with S8R elements and homogenised stiffness.

The stiffness matrix of the plate model has been computed with the polynomial regressions proposed in the previous section. The shell thickness can be arbitrarily defined, the choice of the material density should thus be carefully selected so that the plate surface weight (in N/m^2) remains equal to $\rho g S/H$. In the followings, we compare the strain energy and displacement of the structures.

5.4. Boundary conditions

In both models, the cylinders are clamped, we have $\mathbf{u} = \mathbf{0}$ and $\mathbf{R} = \mathbf{0}$. These conditions are not exactly equivalent, since Poisson effect is restricted on the 3D model, and not in the equivalent plate model. However, the effect should be localised to a few laces and be negligible in the numerical results, due to the large number of laces.

5.5. Convergence

First, a convergence study is conducted in order to guarantee the accuracy of the finite element model. It should be noted that the size of the 3D elements should be small compared to the size of the lace in order to capture the influence of geometrical heterogeneity, as shown in Figure 16, whereas the size of the 2d elements do not depend on the lace dimension, but rather on the curvature of the shell. As a result, the plate model requires far less elements to converge, and this tendency is expected to be amplified as the number of laces increases.

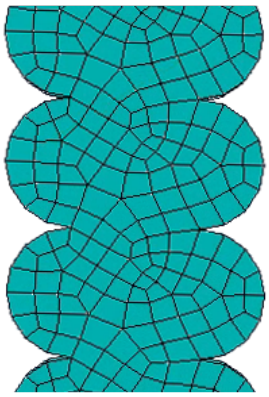

Figure 16: Mesh edges on section of lace in the 3D model upon convergence of the results.

Table 3 shows the convergence of the plate model for both load cases. It can be seen that few degrees of freedom are needed to reach convergence: if we accept a relative error of 1% between the finite element model and a reference solution, only 528 degrees of freedom are required. On the other hand, table 4 shows a slower convergence of the model with 3D elements, with more that $500,000$ degrees of freedom to reach convergence with the same criterion. The 3D model does not seem to have fully converged for load case 2, and further refinements are not possible with an academic license of ABAQUS (limited to 250,000 nodes). This in itself illustrates a practical limit of 3D modelling for complex 3d printed pieces in a realistic printing scenario.

Number of degrees of freedom	384	**528**	2808	5 670	14 784	90 420	182 748	359 040
Strain energy $\mathcal{E}$, LC1 (mJ)	1619.99	**1618.96**	1620.04	1 620.07	1 620.08	1 620.08	1 620.08	1 620.08
Strain energy $\mathcal{E}$, LC2 (mJ)	1672.86	**1676.71**	1682.8	1 683.61	1 684.39	1 685.09	1 685.22	1 685.31
Displacement δ, LC1 (mJ)	37.48	**37.45**	37.44	37.44	37.44	37.44	37.44	37.44
Displacement δ, LC2 (mJ)	48.7	**50.18**	49.85	49.89	49.94	49.97	49.98	49.98
relative error on $\mathcal{E}$, LC1 (-)	0.0%	**0.1%**	0.0%	0.0%	0.0%	0.0%	0.0%	0.0%
relative error on $\mathcal{E}$, LC2 (-)	0.7%	**0.5%**	0.1%	0.1%	0.1%	0.0%	0.0%	0.0%
relative error on δ, LC1 (-)	0.1%	**0.0%**	0.0%	0.0%	0.0%	0.0%	0.0%	0.0%
relative error on δ, LC2 (-)	2.6%	**0.4%**	0.3%	0.2%	0.1%	0.0%	0.0%	0.0%

Table 3: Convergence of strain energy and displacement for LC1 and LC2 of the homogenised plate model. The model for which, 1% deviation with the reference solution is obtained is highlighted in bold numbers.

Number of degrees of freedom	37 458	127 890	181 092	325 125	**580 614**	706 917
Strain energy $\mathcal{E}$, LC1 (mJ)	891.3	1 292.70	1 498.50	1 558.80	**1 585.00**	1 590.80
Strain energy $\mathcal{E}$, LC2 (mJ)	932.889	1 348.65	1 594.42	1 624.30	**1 647.10**	1 662.97
Displacement δ, LC1 (mm)	25.12	31.43	36.14	36.92	**37.29**	37.33
Displacement δ, LC2 (mm)	34.5	42.68	47.91	48.43	**49.66**	49.7
relative error on $\mathcal{E}$, LC1 (-)	44,0%	18.7%	5.8%	2.0%	**0.4%**	0.0%
relative error on $\mathcal{E}$, LC2 (-)	43,9%	18.9%	4.1%	2.3%	**1.0%**	0.0%
relative error on δ, LC1 (-)	32.7%	15.8%	3.2%	1.1%	**0.1%**	0.0%
relative error on δ, LC2 (-)	30,6%	14.1%	3.6%	2.6%	**0.1%**	0.0%

Table 4: Convergence of strain energy and displacement for LC1 and LC2 of the 3D model. The model for which, 1% deviation with the reference solution is obtained is highlighted in bold numbers.

Although a single example should not lead to simplistic generalization, it is clear that the number of degrees of freedom should remain significantly lower for the homogenised solution, since, unlike for conventional 3D models, mesh size is not bounded by lace dimension. For example, in the model with 528 degrees of freedom the typical mesh size is 20 centimeters, 15 times more than the lace dimension. This is in line with previous studies where homogenisation has lower computational complexity [22]. The example shown in this article is far from extreme, with 75 layers, compared to some industrial applications with several hundreds of layers. In this particular example, the plate model requires approximately 500-1000 times less degrees of freedom than the 3D model to converge within the same accuracy in displacement and energy. More complex and localised load cases, like the pressing force exerted by the nozzle [28] would however require adaptive refinement and thus decrease the relative performance of the equivalent plate model with respect to 3D model.

5.6. Accuracy of the homogenised plate model

Strain energy and maximal displacement for the homogenised model (with 359,040 degrees of freedom) and 3D model (with 706,917 degrees of freedom) are compared in order to assess the accuracy of the

homogenisation scheme:

- For load case 1, the relative gap between the converged 3D and plate models is 1.8% on strain energy and 0.3% for displacements.
- For load case 2, the relative gap between the converged 3D and plate models is 1.3% on strain energy and 0.6% for displacements.

Figure 17 shows the deformed geometries of the 3D and plate models for both load cases. Only the displacements of a vertical wall are shown: for the first load case, the displacements are axially-symmetrical and this is representative of the whole deformation; for the second load case, the wall with the highest displacement is chosen. It can be noticed that the displacements are in very good agreement, including the localised curvature occurring near the clamped segment of the cylinder for load case 2.

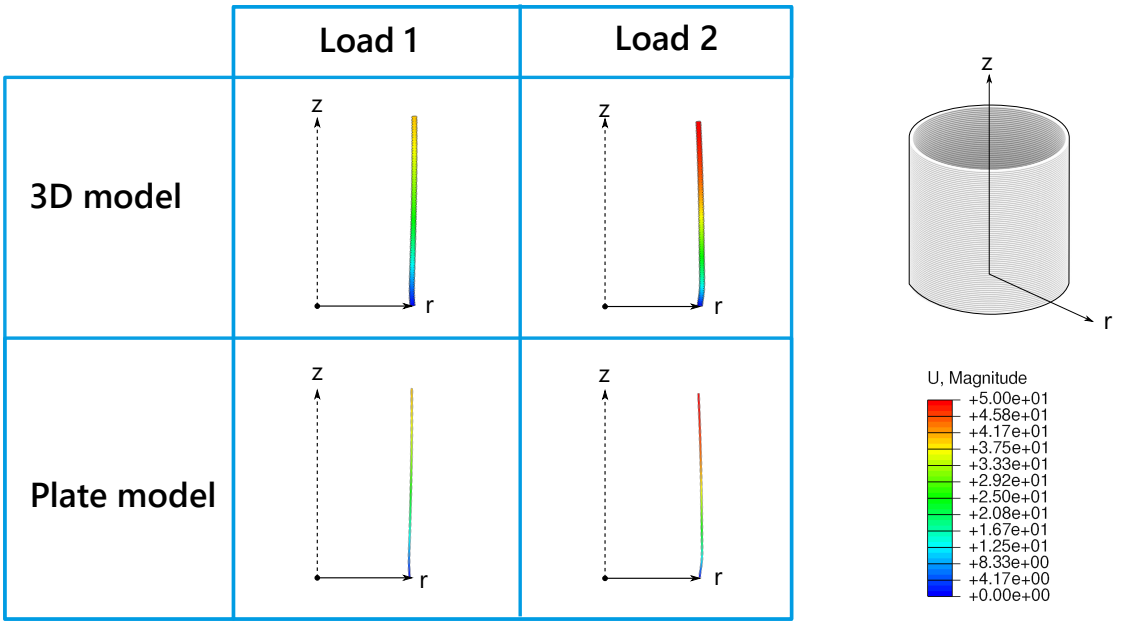

Figure 17: Visualisation of deformed configurations for the 3D model and homogenised model constructed in this article.

Therefore, it can be seen that the homogenisation technique provides good results on practical examples in elasticity. The homogenised model is accurate, despite the shell curvature, which is not accounted for in our homogenisation procedure. The accuracy of the homogenisation is due to the fact that the radius of curvature of the cylinder R remains large compared to the size of the periodic cell. Therefore, the proposed methodology can be used not only for planar periodic plates, but also to curved structures, which are of practical interest with 3d printing.

5.7. Experimental validation

The homogenisation strategy can also be compared to experimental results, although no previous publication estimates all the matrix stiffness of a 3d printed plate. The uniaxial stiffness K along $\mathbf{e_1}$ was experimentally measured by a uniaxial tensile test in [15]. Additionally, the lace dimensions were also retrieved from the same study. The reader is referred to the supplementary material for further details. This allows to estimates the geometrical parameters w^*, as well as material parameters required as input in our model. Figure 18 shows the comparison between those experimental results and the homogenisation, and shows good consistency, within the standard deviation of experimental results. The details on the determination of geometrical parameters for our model, which lead to the construction of this figure are in the supplementary material.

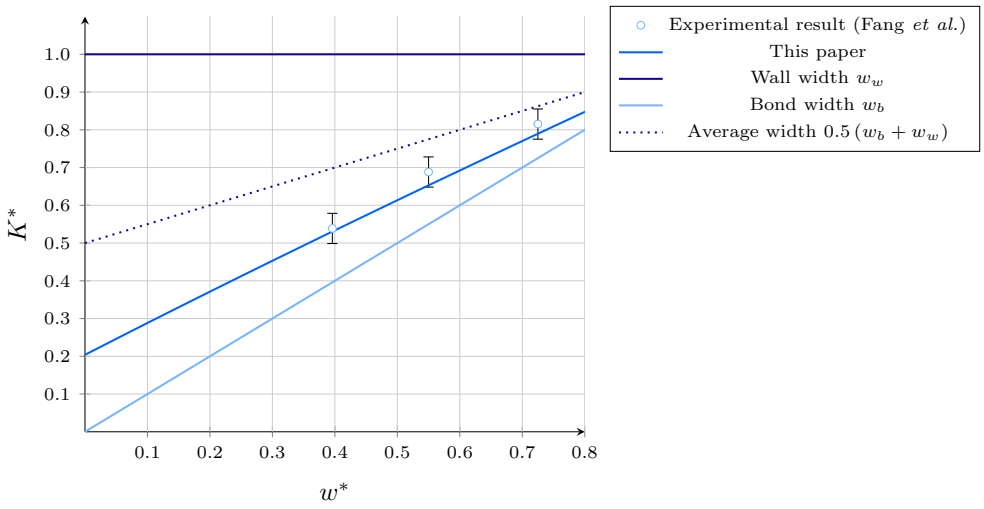

Figure 18: Dimensionless uniaxial stiffness: comparison between [15] and this article.

Interestingly, although Fang *et al.* [15] consider plastic extrusion, and a process involving a phase change, the geometrical model explains most of the orthotropy of the plate. This was already discussed in [15], where the change in Young's modulus for a single filament is less than 2%, whereas the axial stiffness may vary by 40%, as seen in Figure 18. It should also be noted that the equality $H^* = 1 - w^*$ is not fulfilled by experimental results for large values of H^* (superior to 0.35), but our simple model remains accurate. This should be confirmed with experimental results on bending.

6. Discussion

The comparative study has illustrated the accuracy of the homogenisation technique. This section a discussion on practical applications of the proposed methodology to other extrusion strategies with a special focus on 3d concrete printing.

6.1. Sensitivity of axial and bending stiffness to geometrical anisotropy

The homogenisation procedure has illustrated the potential influence of geometrical imperfections at the layer's scale on the stiffness of 3d printed structures. The numerical results show that this influence is much more prevalent for the bending stiffness than for the axial stiffness. This can be understood by two considerations. First, we may look back at the isotropic plate, where bending stiffness scales in $\mathcal{D} \propto w_w^3$ and axial stiffness scales in $\mathcal{A} \propto w_w$: it is clear that a change in thickness will affect the bending stiffness much more than the axial stiffness. Writing $\delta = \varepsilon / w_w$, we have indeed:

$$\begin{cases} \dfrac{\mathcal{D}(w_w) - \mathcal{D}(w_w - \varepsilon)}{\mathcal{D}(w_w)} = & 3\delta - 3\delta^2 + \delta^3 \\ \dfrac{\mathcal{A}(w_w) - \mathcal{A}(w_w - \varepsilon)}{\mathcal{A}(w_w)} = & \delta \end{cases}$$

This simple explanation may illustrate the good accuracy of the linear fit between defect amplitude and A^* components in the homogenisation, and why it is not sufficient for the D^* components. Second, the geometrical defect is distributed along the lace: the extra amount of material acts as a stiffener in the longitudinal direction, while the the transverse bending stiffness mainly depends on the bond width w_b. It therefore natural that D_{1111} converges to 0 as w^* and thus the bond width tend to zero. In such case, the plate structure becomes a juxtaposition of beams with a partial restriction of Poisson's effect.

6.2. Significance of geometrical anisotropy

As indicated in the literature review, material anisotropy has been observed in 3D printed. Keita *et al.* identified drying as the key factor in the material anisotropy, because 3d printed laces are exposed to air [31]. They also show that, the decrease in strength remains inferior to 20% for non-protected material with an interlayer time of 10 minutes, and remains negligible when the 3d printed structures is protected from water loss and the inter-layer time remains inferior to the open time of the mix. To the best of our knowledge, no study seem to investigate the stiffness of 3d printed concrete. By extrapolating data on layer strength, we may however infer that for structures printed with good curing conditions, the geometrical origin of anisotropy is most likely to be the dominant factor explaining structural anisotropy.

6.3. Practical applications to concrete printing

The homogenisation method presented in this article may be applied to linear elastic material. While this framework may seem restrictive for cementitious materials, it is perfectly adapted to other materials with a large elastic domain, such as plastics. The model proposed here also retains practical relevance in 3DCP:

- For stability analysis during printing. It has been shown in [32] that homogenization theory also applied for linearized buckling with good accuracy. Our approach could thus be used to estimate the buckling load of fresh samples during printing. Elastic buckling is indeed the typical failure mode for very slender structures, as recalled in [19]. We consider that studying post-bifurcation behaviour is not relevant from a practical perspective, since the printing can be considered a failure.
- At the fresh state, we can also use this model to evaluate deformation of the piece, similarly to [29].
- For determining natural frequencies of 3d printed structures. This is especially relevant in the case of footbridges, which begin to become more commonplace in 3d printing applications, [9].
- In pre-stressed structures, the elastic domain is more important and our approach could be used to evaluate the structural behaviour of the structure.

In oriented-lace pressing, we can consider a circular nozzle[2] of diameter D. In this situation, existing literature usually mentions the ratio H/D rather than H/w_w. Writing $V^* = V_r/V_e$, the ratio between robot and extrusion velocity, the parameter w_w can be obtained from the mass conservation equation [14]:

$$(w_w - H) \cdot H + \frac{\pi H^2}{4} = \frac{\pi D^2}{4V^*} \tag{29}$$

which yields a relation between H^* and $D^* = D/H$.

$$H^* = \frac{1}{1 + \frac{\pi}{4}\left(\frac{D^{*2}}{V^*} - 1\right)} \tag{30}$$

The value D^* has a lower bound dictated by the force induced by the shaping of one lace. Indeed, the deformation of the lace induces a shear stress proportional to D^{*3}, as shown experimentally in [14], which

[2]Non-circular nozzles can also be used in oriented-lace pressing, in this kind of situation, the material has sufficient yield stress to withstand the weight of one layer and the printing time is long enough to have an evolution of the rheological properties of the mix.

jeopardises the structural integrity of the lowest layers. Practical values for D^* are therefore usually comprised between 1.25 and 5, which is on par with values from [3]. Application of equation (30) yields that H^* is comprised between 0.2 and 0.6. The numerical results show that D_{2222}/D_{1111} varies drastically within this practical range of H^*, from 1.5 to 5. This is mainly due high variations of ${D_{1111}}^*$ with H^*, as illustrated in Figure 13.

6.4. Guidelines for oriented-lace pressing strategy

With this result in mind, some guidelines for printing efficient structures can thus be proposed. Obviously, modifying the toolpath in order to control the lace geometry is possible, but dimensional properties are related by the mass conservation equation. This means that the designer should also modify the geometry of the nozzle together with the layer height.

First, it appears that all terms of the stiffness matrix decrease with H^*. If one considers the effective width B as a design constraint, the best strategy from the unique standpoint of stiffness is to decrease the diameter of the nozzle and to further press the layer, i.e. decreasing H/D. Indeed, equation (29) can be written as $D = \sqrt{V^*}\sqrt{4w_w H/\pi + H^2(1-4/\pi)}$, which decreases with H. Therefore, in order to further press layers, it is necessary to change the diameter of the nozzle. It can be noticed that it is also possible to change the speed of the robot via the parameter V^*, but the influence of this parameter is far less significant than the nozzle diameter (linear vs. quadratic terms in equation (29)). The nozzle size could be adapted either before printing or during printing [33]. There are several obvious limitations to this approach:

- The pressing force increases greatly when H^* decreases, which sets a minimum practical value for H^*, which depends on the thixotropy of the material
- The nozzle diameter cannot be made arbitrarily small, as viscous forces are inversely proportional to D^2 in laminar viscous flow and granular effects are bound to appear in mortars.

Second, one can also opt for a non-circular nozzle, which would result in a more regular lace geometry. Given the very low values of ${D_{1111}}^*$ for high values of H^*, one can indeed consider that using a wide rectangular nozzle would result in oblong laces with low values of H^*, which yield more efficient structures. The main technical difficulty with this technique is the fact that the nozzle orientation has to remain aligned with the lace, which requires an additional axis. This is an undeniable technological complication compared to a simple circular nozzle, but it remains feasible, and is used in extruded lace shaping strategies. To the best of our knowledge, the possibility of using non-circular nozzle with oriented-lace pressing strategies with accelerator is not mentioned in the existing literature: the structural efficiency seems to be a strong

argument to further consider it. Therefore, there is a compromise between structural efficiency and the process complexity to be found. This compromise depends on the final use of the 3d-printed structure.

6.5. Extension of the methodology

6.5.1. Effect of deposition strategy

Although the methodology has been applied to an oblong shape resulting from an *oriented-lace shaping* strategy, it could also be applied to other micro-structures, such as the staggered rectangular sections obtained by printing cantilevers with corbels, shown in Figure 19 [11]. The gap between consecutive layers

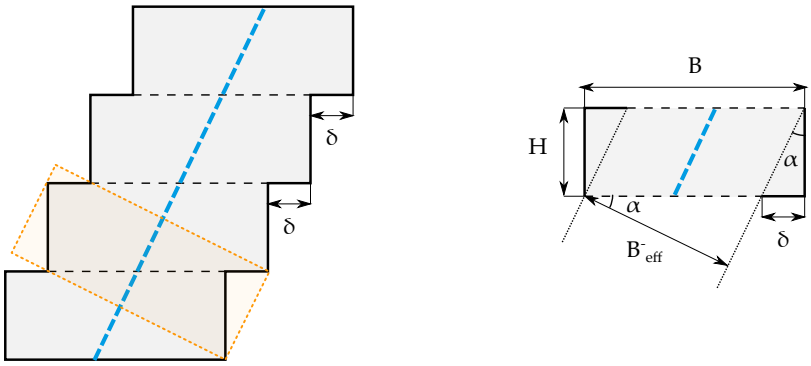

Figure 19: Cross section of a shell extruded with a corbel strategy, often used in infinite brick extrusion (image inspired by [11]). The middle surface is highlighted in dashed blue lines, and a periodic cell is shown in orange.

δ is expected to reduce the contact between laces B^{-}_{eff}, and the overall stiffness, as seen in Figure 19. Small geometrical irregularities arise from the successive gap between layers. Contrary to the case treated in this article, it is not possible to find a periodic cell with two planes of symmetry, which may indicate a coupling between axial forces and bending. However, homogenisation remains applicable to evaluate the stiffness properties of such structures if the variation of the gap δ between successive layers remains small compared to the typical dimensions of the unit cell H. Based on the result obtained for the oblong shape, the bending stiffness can be expected to drop significantly as the slope α increases.

6.5.2. Material heterogeneity

The objective of this article being to understand the influence of geometrical parameters on the stiffness of 3d-printed structures, our approach considered a uniform material. Phenomena, like loss of stiffness at the interface that would come from cold joints can easily be integrated in the proposed methodology and could refine the understanding of influence of cold-joints at the structural scale and not only at the lace scale.

6.5.3. Towards local/global modelling

In this contribution, the proposed methodology is applied to an analytical shape for the lace, which is in good accordance with experimental data, but it could be applied to other shapes that are experimentally measured [12] or simulated. A link between an affordable local simulation at the nozzle scale and a global simulation using homogenisation is thus a promising research direction for efficient simulation of 3D printing process.

So far, the homogenisation has been applied to a uniform material. It is possible to construct a model where the stiffness properties are derived from the homogenised model and the time-dependent material properties. However, the relative contrast between the material properties of successive layers should remain small in order to maintain applicability of the model. The accuracy of the homogenised model may thus decrease when modelling structures printed with materials with a large structuration rate, especially near the nozzle exit. This should be investigated in further research.

7. Conclusion

The aim of this paper was to propose a methodology to assess the geometrical influence of the lace geometry on the stiffness of 3d printed structures. To do so, we considered a homogeneous material and eliminated the eventual influence of weak interfaces or "cold joints". A numerical homogenisation procedure allowing to construct an equivalent orthotropic Kirchhoff-Love plate has been proposed. It leverages the theory of periodic homogenisation, which is well established and seems particularly adequate in 3d printing: the structures are (pseudo)-periodic, with a large number of cells, which guarantees a convergence of the homogenised model to the "real" solution of the 3D problem.

Even in the assumption of a perfect interface between layers, the homogenisation procedure highlights a significant anisotropy of 3d printed structures with a lace geometry similar to those obtained by pressing of a circular lace. The ratio between longitudinal and transversal bending stiffness was found to be superior to 150% for usual dimensional values of laces obtained by oriented layer pressing. The anisotropy of the membrane stiffness is less pronounced, but should still be measurable experimentally. This study confirms that even in favorable conditions for the inter-layer binding, a geometrical origin of anisotropy in some 3d-printed structures should still be accounted for. These numerical and theoretical results could be experimentally tested, for example with the method introduced in [34], which allows to measure all terms of the stiffness matrix.

The proposed model can readily be used for pre-stressed concrete structures or for process simulation,

with a significant speed-up compared to 3D modelling. More importantly, the homogenisation scheme provides a deeper understanding of the geometrical origin of anisotropy in concrete structures, allowing to separate the influence of material (micro-scale) and the influence of the deposition process (meso-scale) on the behaviour of the structure (macro-scale).

Although the numerical focus was on circular nozzles and oriented lace pressing, the proposed methodology can be extended to other configurations typically found in 3d concrete printing, like staggered rectangular layers. Future work could also include a weak layer at the interface in order to assess the influence of cold-joints on the overall structural behaviour. Finally, homogenisation can also be used to determine the yield domain of structures: applications of these methods would pave the way to efficient implementations of nonlinear finite element plate models for 3d printed structures.

References

[1] J. Pegna, Exploratory investigation of solid freeform construction, Automation in construction 5 (5) (1997) 427–437.

[2] B. Khoshnevis, Automated construction by contour crafting—related robotics and information technologies, Automation in Construction 13 (1) (2004) 5–19, the best of ISARC 2002. doi:https://doi.org/10.1016/j.autcon.2003.08.012.
URL https://www.sciencedirect.com/science/article/pii/S0926580503000736

[3] S. Lim, R. Buswell, T. Le, S. Austin, A. Gibb, T. Thorpe, Developments in construction-scale additive manufacturing processes, Automation in Construction 21 (2012) 262 – 268. doi:https://doi.org/10.1016/j.autcon.2011.06.010.
URL http://www.sciencedirect.com/science/article/pii/S0926580511001221

[4] Y. W. D. Tay, G. H. A. Ting, Y. Qian, B. Panda, L. He, M. J. Tan, Time gap effect on bond strength of 3d-printed concrete, Virtual and Physical Prototyping 14 (1) (2019) 104–113. arXiv:https://doi.org/10.1080/17452759.2018.1500420, doi:10.1080/17452759.2018.1500420.
URL https://doi.org/10.1080/17452759.2018.1500420

[5] P. Margerit, D. Weisz-Patrault, K. Ravi-Chandar, A. Constantinescu, Tensile and ductile fracture properties of as-printed 316l stainless steel thin walls obtained by directed energy deposition, Additive Manufacturing 37 (2021) 101664. doi:https://doi.org/10.1016/j.addma.2020.101664.
URL https://www.sciencedirect.com/science/article/pii/S2214860420310368

[6] V. N. Nerella, S. Hempel, V. Mechtcherine, Effects of layer-interface properties on mechanical performance of concrete elements produced by extrusion-based 3d-printing, Construction and Building Materials 205 (2019) 586–601. doi:https://doi.org/10.1016/j.conbuildmat.2019.01.235.
URL https://www.sciencedirect.com/science/article/pii/S0950061819302843

[7] N. Roussel, F. Cussigh, Distinct-layer casting of scc: The mechanical consequences of thixotropy, Cement and Concrete Research 38 (5) (2008) 624–632. doi:https://doi.org/10.1016/j.cemconres.2007.09.023.
URL https://www.sciencedirect.com/science/article/pii/S0008884607002426

[8] R. Duballet, R. Mesnil, N. Ducoulombier, P. Carneau, L. Demont, M. Motamedi, O. Baverel, J.-F. Caron, J. Dirrenberger, Free deposition printing for space truss structures, RILEM Bookseries 28 (2020) 873–882, cited By 3. doi:

10.1007/978-3-030-49916-7_85.
URL https://www.scopus.com/inward/record.uri?eid=2-s2.0-85088265022&doi=10.1007%2f978-3-030-49916-7_85&partnerID=40&md5=4477ba5d6d0964d4173c1a3e87600614

[9] T. A. Salet, Z. Y. Ahmed, F. P. Bos, H. L. Laagland, Design of a 3d printed concrete bridge by testing, Virtual and Physical Prototyping 13 (3) (2018) 222–236.

[10] C. Gosselin, R. Duballet, P. Roux, N. Gaudillière, J. Dirrenberger, P. Morel, Large-scale 3d printing of ultra-high performance concrete–a new processing route for architects and builders, Materials & Design 100 (2016) 102–109.

[11] P. Carneau, R. Mesnil, N. Roussel, O. Baverel, Additive manufacturing of cantilever - from masonry to concrete 3d printing, Automation in Construction 116 (2020) 103184. doi:https://doi.org/10.1016/j.autcon.2020.103184.
URL http://www.sciencedirect.com/science/article/pii/S0926580519308568

[12] R. Comminal, M. P. Serdeczny, D. B. Pedersen, J. Spangenberg, Numerical modeling of the strand deposition flow in extrusion-based additive manufacturing, Additive Manufacturing 20 (2018) 68 – 76. doi:https://doi.org/10.1016/j.addma.2017.12.013.
URL http://www.sciencedirect.com/science/article/pii/S2214860417305079

[13] M. P. Serdeczny, R. Comminal, D. B. Pedersen, J. Spangenberg, Experimental validation of a numerical model for the strand shape in material extrusion additive manufacturing, Additive Manufacturing 24 (2018) 145 – 153. doi:https://doi.org/10.1016/j.addma.2018.09.022.
URL http://www.sciencedirect.com/science/article/pii/S2214860418304585

[14] P. Carneau, R. Mesnil, O. Baverel, N. Roussel, Layer pressing in concrete extrusion-based 3d-printing: Experiments and analysis, Cement and Concrete Research 155 (2022) 106741. doi:https://doi.org/10.1016/j.cemconres.2022.106741.
URL https://www.sciencedirect.com/science/article/pii/S0008884622000321

[15] L. Fang, Y. Yan, O. Agarwal, J. E. Seppala, K. D. Migler, T. D. Nguyen, S. H. Kang, Estimations of the effective young's modulus of specimens prepared by fused filament fabrication, Additive Manufacturing 42 (2021) 101983. doi:https://doi.org/10.1016/j.addma.2021.101983.
URL https://www.sciencedirect.com/science/article/pii/S2214860421001482

[16] B. Khoshnevis, D. Hwang, K.-T. Yao, Z. Yeh, Mega-scale fabrication by contour crafting, International Journal of Industrial and Systems Engineering 1 (3) (2006) 301–320.

[17] R. Duballet, O. Baverel, J. Dirrenberger, Classification of building systems for concrete 3d printing, Automation in Construction 83 (2017) 247 – 258. doi:https://doi.org/10.1016/j.autcon.2017.08.018.
URL http://www.sciencedirect.com/science/article/pii/S0926580516302977

[18] A. Suiker, Mechanical performance of wall structures in 3d printing processes: Theory, design tools and experiments, International Journal of Mechanical Sciences 137 (2018) 145 – 170. doi:https://doi.org/10.1016/j.ijmecsci.2018.01.010.
URL http://www.sciencedirect.com/science/article/pii/S0020740317330370

[19] A. Suiker, R. Wolfs, S. Lucas, T. Salet, Elastic buckling and plastic collapse during 3d concrete printing, Cement and Concrete Research 135 (2020) 106016. doi:https://doi.org/10.1016/j.cemconres.2020.106016.
URL http://www.sciencedirect.com/science/article/pii/S0008884620300946

[20] T. Ooms, G. Vantyghem, R. Van Coile, W. De Corte, A parametric modelling strategy for the numerical simulation of 3d concrete printing with complex geometries, Additive Manufacturing 38 (2021) 101743. doi:https://doi.org/10.1016/j.

addma.2020.101743.
URL http://www.sciencedirect.com/science/article/pii/S2214860420311155

[21] G. Vantyghem, T. Ooms, W. De Corte, Voxelprint: A grasshopper plug-in for voxel-based numerical simulation of concrete printing, Automation in Construction 122 (2021) 103469. doi:https://doi.org/10.1016/j.autcon.2020.103469.
URL http://www.sciencedirect.com/science/article/pii/S0926580520310499

[22] K. Sab, A. Lebée, Homogenization of heterogeneous thin and thick plates, John Wiley & Sons, 2015.

[23] P. Winslow, S. Pellegrino, S. Sharma, Multi-objective optimization of free-form grid structures, Structural and multidisciplinary optimization 40 (1) (2010) 257–269.

[24] R. Mesnil, C. Douthe, O. Baverel, B. Léger, Linear buckling of quadrangular and kagome gridshells: A comparative assessment, Engineering Structures 132 (2017) 337–348. doi:https://doi.org/10.1016/j.engstruct.2016.11.039.
URL https://www.sciencedirect.com/science/article/pii/S0141029616313141

[25] A. Lebée, K. Sab, Homogenization of a space frame as a thick plate: Application of the bending-gradient theory to a beam lattice, Computers Structures 127 (2013) 88–101, special Issue IASS-IACM-2012. doi:https://doi.org/10.1016/j.compstruc.2013.01.011.
URL https://www.sciencedirect.com/science/article/pii/S0045794913000321

[26] B. V. Wilding, M. Godio, K. Beyer, The ratio of shear to elastic modulus of in-plane loaded masonry, Materials and Structures 53 (2) (2020) 1–18.

[27] A. Lebée, K. Sab, Homogenization of thick periodic plates: Application of the bending-gradient plate theory to a folded core sandwich panel, International Journal of Solids and Structures 49 (19) (2012) 2778–2792, proceedings of International Union of Theoretical and Applied Mechanics Symposium. doi:https://doi.org/10.1016/j.ijsolstr.2011.12.009.
URL https://www.sciencedirect.com/science/article/pii/S0020768311004173

[28] P. Carneau, R. Mesnil, N. Ducoulombier, N. Roussel, O. Baverel, Characterisation of the layer pressing strategy for concrete 3d printing, in: F. P. Bos, S. S. Lucas, R. J. Wolfs, T. A. Salet (Eds.), Second RILEM International Conference on Concrete and Digital Fabrication, Springer International Publishing, Cham, 2020, pp. 185–195.

[29] J. Archez, S. Maitenaz, L. Demont, M. Charrier, R. Mesnil, N. Texier-Mandoki, X. Bourbon, S. Rossignol, J. Caron, Strategy to shape, on a half-meter scale, a geopolymer composite structure by additive manufacturing, Open Ceramics (2021) 100071doi:https://doi.org/10.1016/j.oceram.2021.100071.
URL https://www.sciencedirect.com/science/article/pii/S2666539521000171

[30] R. Wolfs, F. Bos, T. Salet, Early age mechanical behaviour of 3d printed concrete: Numerical modelling and experimental testing, Cement and Concrete Research 106 (2018) 103–116. doi:https://doi.org/10.1016/j.cemconres.2018.02.001.
URL https://www.sciencedirect.com/science/article/pii/S000888461730532X

[31] E. Keita, H. Bessaies-Bey, W. Zuo, P. Belin, N. Roussel, Weak bond strength between successive layers in extrusion-based additive manufacturing: measurement and physical origin, Cement and Concrete Research 123 (2019) 105787. doi:https://doi.org/10.1016/j.cemconres.2019.105787.
URL https://www.sciencedirect.com/science/article/pii/S0008884618313760

[32] O. Perret, A. Lebée, C. Douthe, K. Sab, The bending–gradient theory for the linear buckling of thick plates: Application to cross laminated timber panels, International Journal of Solids and Structures 87 (2016) 139–152. doi:https://doi.org/10.1016/j.ijsolstr.2016.02.021.
URL https://www.sciencedirect.com/science/article/pii/S0020768316000834

[33] J. Xu, L. Ding, L. Cai, L. Zhang, H. Luo, W. Qin, Volume-forming 3d concrete printing using a variable-size square nozzle, Automation in Construction 104 (2019) 95–106. doi:https://doi.org/10.1016/j.autcon.2019.03.008.
URL https://www.sciencedirect.com/science/article/pii/S0926580518307726

[34] P. Margerit, T. Gobin, A. Lebée, J.-F. Caron, The robotized laser doppler vibrometer: On the use of an industrial robot arm to perform 3d full-field velocity measurements, Optics and Lasers in Engineering 137 (2021) 106363. doi:https://doi.org/10.1016/j.optlaseng.2020.106363.
URL https://www.sciencedirect.com/science/article/pii/S0143816620305509

Appendix A. Analytical expressions of cross-section

Appendix A.1. Analytical expression for S

The cross-section area of the oblong shape is simply given by adding the area of a rectangle of lengths $B - H$ and H and two half-disks of diameter H:

$$S = BH + \left(\frac{\pi}{4} - 1\right) H^2 \tag{A.1}$$

The quantity $S/(BH)$, which appears in (20) is thus:

$$\frac{S}{BH} = 1 + \left(\frac{\pi}{4} - 1\right) H^* \tag{A.2}$$

Appendix A.2. Analytical expression for I

The second moment of area of the cross section is calculated using the parallel axis theorem and by introducing the second moment area $I_{half-disk}$ of a half-disk and d_G, the distance between the center of mass of the half-disk to the axis ($x_1 = 0$).

$$I = 2 \cdot I_{half-disk} + 2S_{half-disk} \cdot d_G^2 + I_{rectangle} \tag{A.3}$$

It can be shown that $d_G = \frac{B-H}{2} + \frac{2H}{3\pi}$,

$$\begin{aligned} I_{half-disk} &= \int_{r=0}^{H/2} \int_{\theta=\frac{-\pi}{2}}^{\frac{\pi}{2}} \left(r\cos\theta - d_G\right)^2 r \mathrm{d}r\mathrm{d}\theta \\ I_{half-disk} &= \frac{H^4}{16}\left(\frac{\pi}{8} - \frac{8}{9\pi}\right) \end{aligned} \tag{A.4}$$

Finally, we get an analytical solution for I.

$$I = \frac{H^4}{8}\left(\frac{\pi}{8} - \frac{8}{9\pi}\right) + \frac{\pi H^2}{4} \cdot \left(\frac{B-H}{2} + \frac{2H}{3\pi}\right)^2 + \frac{H\left(B-H\right)^3}{12} \tag{A.5}$$

The non-dimensional number $\frac{12I}{BH^3}$ appearsin (20). The analytical value for this number follows immediately:

$$\begin{aligned}\frac{12I}{BH^3} =& {H^*}^3\left(\frac{3\pi}{16} - \frac{12}{9\pi}\right) \\ &+ 3\pi H^* \cdot \left(\frac{1}{2} + \left(\frac{2}{3\pi} - \frac{1}{2}\right)H^*\right)^2 \\ &+ \left(1 - H^*\right)^3\end{aligned} \tag{A.6}$$

Appendix B. Numerical results

Follow tables sum up the numerical results of the Finite Element Analysis.

	$\nu = 0.15$	$\nu = 0.2$	$\nu = 0.25$	$\nu = 0.3$
$H^* = 0.05$	0.959	0.957	0.958	0.958
$H^* = 0.25$	0.791	0.791	0.791	0.791
$H^* = 0.50$	0.582	0.582	0.582	0.582
$H^* = 0.75$	0.387	0.387	0.387	0.387
$H^* = 0.95$	0.226	0.226	0.225	0.225

Table B.5: Numerical results of ${A_{1111}}^*$.

	$\nu = 0.15$	$\nu = 0.2$	$\nu = 0.25$	$\nu = 0.3$
$H^* = 0.05$	0.970	0.969	0.969	0.969
$H^* = 0.25$	0.846	0.846	0.846	0.847
$H^* = 0.50$	0.687	0.687	0.687	0.688
$H^* = 0.75$	0.524	0.524	0.525	0.526
$H^* = 0.95$	0.375	0.376	0.379	0.380

Table B.6: Numerical results of ${A_{1212}}^*$.

670

	$\nu = 0.15$	$\nu = 0.2$	$\nu = 0.25$	$\nu = 0.3$
$H^* = 0.05$	0.990	0.987	0.987	0.987
$H^* = 0.25$	0.943	0.940	0.937	0.932
$H^* = 0.50$	0.886	0.880	0.873	0.865
$H^* = 0.75$	0.829	0.821	0.811	0.798
$H^* = 0.95$	0.783	0.773	0.760	0.745

Table B.7: Numerical results for ${A_{2222}}^*$

	$\nu = 0.15$	$\nu = 0.2$	$\nu = 0.25$	$\nu = 0.3$
$H^* = 0.05$	0.880	0.880	0.880	0.880
$H^* = 0.25$	0.498	0.498	0.498	0.498
$H^* = 0.50$	0.208	0.208	0.208	0.208
$H^* = 0.75$	0.059	0.059	0.059	0.059
$H^* = 0.95$	0.003	0.003	0.003	0.003

Table B.8: Numerical results for ${D_{1111}}^*$

	$\nu = 0.15$	$\nu = 0.2$	$\nu = 0.25$	$\nu = 0.3$
$H^* = 0.05$	0.912	0.912	0.913	0.913
$H^* = 0.25$	0.630	0.630	0.630	0.630
$H^* = 0.50$	0.407	0.407	0.407	0.407
$H^* = 0.75$	0.300	0.300	0.300	0.300
$H^* = 0.95$	0.289	0.289	0.289	0.289

Table B.9: Numerical results for ${D_{1212}}^*$

	$\nu = 0.15$	$\nu = 0.2$	$\nu = 0.25$	$\nu = 0.3$
$H^* = 0.05$	0.997	0.965	0.963	0.961
$H^* = 0.25$	0.848	0.842	0.834	0.824
$H^* = 0.50$	0.731	0.722	0.710	0.695
$H^* = 0.75$	0.642	0.632	0.619	0.602
$H^* = 0.95$	0.588	0.577	0.564	0.547

Table B.10: Numerical results for ${D_{2222}}^*$

Appendix C. Polynomial approximation

The result of the linear approximation of numerical results are shown in Table C.11. For axial stiffness, linear regression have been preferred, since they already provide accurate estimation. For bending stiffness, quadratic approximation in (H^*, ν) are chosen. The regressions show that the influence of ν is negligible for the estimation of the dimensionless numbers (the coefficients for ν are two or three orders of magnitude smaller than those for H^*). However, it does not mean that the stiffness matrix is not influenced by ν, because Poisson's ratio is alreay factored in the dimensionless numbers.

	Polynomial approximation	R^2	max error %
${A_{1111}}^*$	$1 - 0.81H^* - 0.001\nu$	0.9998	0.6%
${A_{1212}}^*$	$1 - 0.65H^* + 0.009\nu$	0.9990	1.0%
${D_{1111}}^*$	$1 - 2.11H^* - 0.0007\nu + 1.16{H^*}^2 + 0.00005H^*\nu + 0.001\nu^2$	0.997	2.0%
${D_{1212}}^*$	$1 - 1.68H^* - 0.0003\nu + 0.99{H^*}^2 + 0.0005H^*\nu + 0.0002\nu^2$	0.9992	0.9%

Table C.11: Polynomial regression for the numerical data with R^2 and maximal error.